ISIJ International, Vol. 65 (2025), No. 8, pp. 1231–1238
https://doi.org/10.2355/isijinternational.ISIJINT-2025-049

Microstructural Characteristics of Modified 9Cr-1Mo Steel with Low Creep Ductility

Nobuaki SEKIDO,[1)]* Haruka NAGAI,[1)] Tomotaka HATAKEYAMA,[2)] Kyosuke YOSHIMI[1)] and Kota SAWADA[2)]

1) Graduate School of Engineering, Tohoku University, 6-6-02, Aramaki Aza Aoba, Aoba-ku, Sendai, Miyagi, 980-8579 Japan.
2) National Institute for Materials Science, 1-2-1, Sengen, Tsukuba, Ibaraki, 305-0047, Japan.

(*Received February 26, 2025; Accepted May 7, 2025; Advance online published May 15, 2025; Published July 15, 2025*)

Microstructures of the two heats of Modified 9Cr-1Mo steel that exhibit comparable creep strength but largely different creep ductility were analyzed to identify the factors that can reduce their creep ductility. The critical difference between the microstructures of the two heats was the size and distribution of prior austenite grains (PAGs). For the heat with higher creep ductility, the size of the PAGs was ordinary, approximately 20 μm. In contrast, the microstructure of the heat with low creep ductility was characterized as a mixture of regions with ordinary-sized PAGs and extraordinary coarsened PAGs of several hundred micrometers. The creep deformation of the heat with low creep ductility was found to localize in the regions with ordinary-sized PAGs, which led to the development of creep cavities and cracks, eventually reducing the creep ductility.

KEY WORDS: ferritic heat-resistant steel; creep ductility; microstructure; EBSD; prior-austenite grain.

1. Introduction

Modified 9Cr-1Mo steel (ASME T91/P91) has been used in thermal power plants because of its excellent combination of high thermal conductivity, low thermal expansion coefficient, low susceptibility to thermal fatigue, and good creep strength.[1,2)] Mod. 9Cr-1Mo steel exhibits a typical lath martensitic microstructure, and the stability of sub-boundaries, such as lath and block boundaries, has a significant impact on its creep strength.[3)] The stability of these sub-boundaries is closely related to precipitates that form during creep. Carbide precipitates such as $M_{23}C_6$ and MX contribute to enhancing creep strength by suppressing the recovery and coarsening of the sub-boundaries, as well as by impeding dislocation gliding as the precipitation hardening.[3,4)] On the other hand, the precipitation of Z-phase (Cr(Nb,V)N) or Laves phase (Fe_2Mo) is known to cause the dissolution of fine-scaled MX precipitates during creep, which leads to a loss of creep strength in the prolonged time regime.[5,6)]

Recently, the increasing use of renewable energy has been accompanied by the increase in frequent cycle and load-following operations in coal-fired power plants, which leads to growing concerns about failure accidents of steam pipes caused by creep-fatigue.[7)] It is accepted that creep-fatigue life is reduced when creep ductility is reduced in ferritic heat-resistant steels, as well as in austenitic heat-resistant steels and Ni-based superalloys.[8)] Thus, knowledge of the microstructural features that can reduce the creep ductility of ferritic steels will contribute to securing the safety and reliability of the power plants.

Fortunately, Mod. 9Cr-1Mo steel is one of the most well-studied creep-strength-enhanced ferritic (CSEF) steels with respect to long-term creep life. One good example would be the “Creep Data Sheet project” led by the National Institute for Materials Science (NIMS) Japan, which has provided extensive creep data of prolonged lives longer than 100 000 hours for various heat-resistant steels and heat-resistant alloys,[9)] including the Mod. 9Cr-1Mo steel.[10)] Although Mod. 9Cr-1Mo steel is generally ductile, there are some “heats” that have been reported to show low creep ductility, *i.e.*, low failure strain and low reduction of area at rupture.[10–12)] Note that “heat” denotes an individual steel sample that meets the specification requirements but has slight differences in composition and/or substructure due to different manufacturers.

This study focuses on two heats of Mod. 9Cr-1Mo steel from the NIMS Creep Data Sheet, MGQ and MGS, which exhibit comparable creep strength but markedly different creep ductility. Microstructural analyses were performed on pre- and post-creep specimens of the two heats to identify the damage initiation and development processes. The microstructural factors that affect creep ductility are clarified by comparing the two heats.

---

* Corresponding author: E-mail: sekido@material.tohoku.ac.jp

2. Experimental Procedures

The present study focused on the two heats of Mod. 9Cr-1Mo steel pipes, which are hereafter denoted as MGQ and MGS in accordance with the NIMS Creep Data Sheet.[10] The chemical compositions of the two heats are summarized in **Table 1**. Recently, it has been reported that impurity elements such as Al, Cu, S, As, Sb, and Sn can reduce the creep ductility of Mod. 9Cr-1Mo steel.[12] The concentrations of these harmful elements are sufficiently low in both MGS and MGQ, as shown in Table 1.

MGQ was hot-worked into a pipe with an outside diameter of 335 mm and a wall thickness of 35.7 mm. MGQ was normalized at 1 060°C for 1 h, followed by tempering at 780°C for 1 h. On the other hand, MGS was hot-worked into a pipe with an outside diameter of 406 mm and a wall thickness of 90 mm. MGS was normalized at 1 050°C for 0.5 h, then tempered at 780°C for 1 h. MGS was further annealed by twice steps of 745°C for 5 h to reproduce PWHT (Post Weld Heat Treatment).

The microstructures of as-received and crept samples were analyzed by optical microscope (OM), field-emission scanning electron microscope (FE-SEM), electron backscattered diffraction (EBSD), high-resolution low-voltage SEM, transmission electron microscope (TEM), scanning transmission electron microscope (STEM), and energy-dispersive X-ray spectroscopy (EDS). OM specimens were mechanically polished up to 0.1 μm of alumina slurry. Nital solution, as well as Vilella's reagent, was used for etching in this study because prior austenite grain boundaries were more clearly visualized with the Nital solution. Although MX is known to be as small as a few tens of nm, it has been shown that 10 nm of MX can be visualized by using a high-resolution low-voltage SEM together with appropriate surface finishing.[13] In this study, the specimens for low-voltage SEM observation were mechanically polished to 0.1 μm and the surface was finished by an ion milling system. The EBSD data were processed using the EDAX OIM Analysis software (ver. 8.6) for the reconstruction of prior austenite grains. TEM and STEM specimens were prepared using the focused ion beam (FIB) micro-sampling technique. Mechanical properties of the local areas were evaluated by Micro-Vickers hardness with a load of 0.01 kgf.

3. Results

3.1. Creep Behavior

Figure 1 summarizes the results of creep tests conducted on MGQ and MGS at temperatures of 600, 625, and 650°C under the applied stresses ranging from 50 to 180 MPa. The stress rupture curves shown in Fig. 1(a) indicate that MGQ and MGS have comparable creep strength in the temperature range of 600°C to 650°C. However, their rupture elongation (Fig. 1(b)) and reduction of area at rupture (Fig. 1(c)) exhibit quite different trends: MGQ exhibits larger elongation and higher reduction of area, while MGS is less ductile, particularly in the low-stress regime.

In general, the creep damage tolerance factor λ is an indicator to assess the susceptibility to localized cracking upon strain concentrations,[14,15] and is defined as the ratio of the failure strain to the secondary creep strain as follows:

$$\lambda = \frac{\varepsilon_f}{\dot{\varepsilon}_{min} t_r} \quad \text{.................................} (1)$$

, where ε_f is the failure strain, $\dot{\varepsilon}_{min}$ is the minimum strain rate, and t_r is the time to rupture. It is noted that a value of λ larger

Table 1. Chemical compositions of the MGQ and MGS (in mass.%).

	C	Si	Mn	P	S	Cu	Ni	Cr	Mo	V
MGQ	0.11	0.24	0.43	0.014	0.002	0.016	0.08	8.31	0.92	0.19
MGS	0.10	0.32	0.45	0.01	0	0.013	0.12	8.90	0.91	0.20
	Nb	Al	N	W	Ti	Zr	B	As	Sn	Sb
	0.07	0.001	0.046	0.001	0.005	<0.001	<0.001	0.004	0.0004	0.0004
	0.07	0.009	0.050	<0.003	<0.003	<0.003	<0.0001	<0.003	<0.003	<0.003

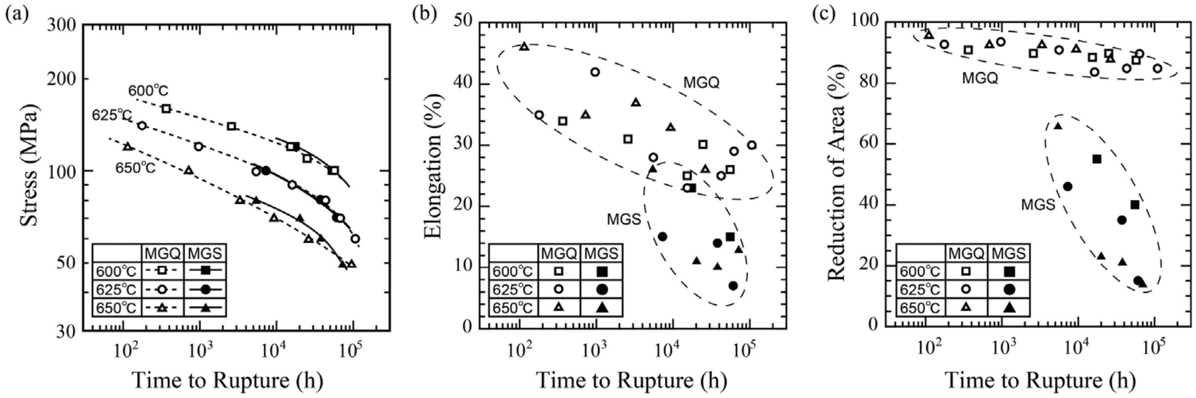

Fig. 1. Summary of creep tests conducted on MGQ and MGS at 600°C, 625°C, and 650°C under stresses ranging from 60 MPa to 180 MPa. (a) stress vs. rupture time, (b) rupture elongation, and (c) reduction of area at rupture.

than 5 is generally sufficient to ensure that the local strain levels that typically occur in service do not lead to premature cracking.[16] According to the ASME code,[17] materials with a value of λ smaller than 5 are classified as creep-intolerant, necessitating a reduction in the allowable stress. The values of λ for MGQ were found to range from 10 to 15, while that for MGS was 5.1 at its lowest value, suggesting that MGS is less ductile than conventional Mod. 9Cr-1Mo steel but not too brittle in terms of the damage tolerance factor.

3.2. Prior Austenite Grain Structure and Damage Development during Creep

Figure 2 shows optical micrographs, EBSD-IPF (inverse pole figure) maps, and the corresponding austenite reconstruction images of as-received MGQ and MGS. As shown in the optical micrographs (Figs. 2(a) and 2(d)) and EBSD-IPF maps (Figs. 2(b) and 2(e)), both MGS and MGQ exhibit typical lath martensitic microstructures, but the length of martensite blocks in MGS appear to be longer than that in MGQ. Recently, it has been demonstrated that inverse analysis to reconstruct austenite grains from martensite grain orientation information obtained by EBSD yields reliable results.[18–20] Since the prior austenite grain boundary (PAGB) was not clearly identified by optical micrographs, particularly in MGS, PAGBs were identified by reconstructing austenite grains from EBSD data using the OIM software. In 9Cr heat-resistant steels, several orientation relationships have been reported to occur between the martensite and austenite phases,[21] while the most frequently observed are Kurdjumov-Sachs (K-S)[22] and Nishiyama-Wassermann (N-W)[23] relationships. In this study, both orientation relationships were examined for the reconstruction of prior austenite grains. However, the results of the two models were not significantly different, and obvious misinterpretations were fewer when the N-W relationship was assumed. Thus, in this study, the reconstruction of austenite grains from EBSD data was carried out using the N-W model.

The austenite grain reconstruction maps of MGQ and MGS are shown in Figs. 2(c) and 2(f). A clear difference between the two is the sizes of prior austenite grains (PAGs). For MGQ, the size of PAGs is uniform with an average size of about 20 μm. For MGS, on the other hand, PAGs are non-uniform in size, ranging from 20 μm to about 1 mm. A PAG size of about 20 μm is an ordinary value often observed in Mod. 9Cr-1Mo steel after normalizing and tempering,[10,24] and such a region is hereafter denoted as a "normal-sized PAG region". On the other hand, the region of extraordinary coarsened PAG sizes as large as several hundred μm is referred to "abnormal-sized PAG region".

Figure 3 shows the cross-sectional macrographs on the tip of the fractured creep specimens tested at 650°C under the stress of 60 MPa. The rupture times for MGQ and MGS were 26 187 h and 38 108 h, respectively. As mentioned previously, MGQ is so ductile that the reduction of area at rupture reaches 80% or higher as shown in Fig. 1(c), which results in the development of grains elongated along the stress direction near the tip. PAG reconstruction was not successful for the crept MGQ specimen because recrystallization occurred near the tip of the ruptured specimen. On the other hand, such elongated grains as in Fig. 3(c) were not observed in the crept MGS specimen, and a reasonable PAG reconstruction was possible as in Fig. 2(c). What is interesting is that cavity development is only observed in the normal-sized PAG region. This trend is evidentially manifested in the large-scale EBSD results. **Figure 4** shows the EBSD-IPF map and its PAG reconstruction of the crept MGS specimen ruptured in 38 108.9 h at 650°C under the stress of 60 MPa. This EBSD image was taken from an extensive area of 3×10 (mm) with a step size of 1 μm, which is sufficiently small for PAG analysis. As noted above it is obvious that the occurrence of cavities can be confirmed only in the normal-sized PAG regions. These results suggest that creep deformation was localized in the normal-sized PAG regions, which then resulted in the lower creep ductility of MGS.

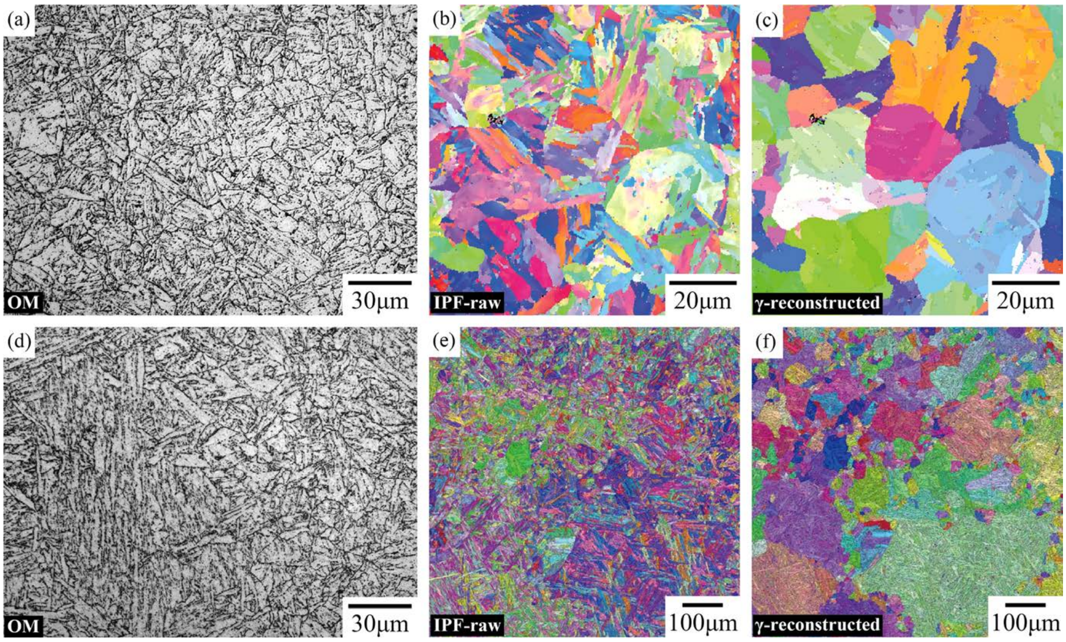

Fig. 2. Optical micrographs (a, d), EBSD-IPF maps (b, e), and austenite reconstruction maps (c, f) of MGQ (a–c) and MGS (d–f) specimens. (Online version in color.)

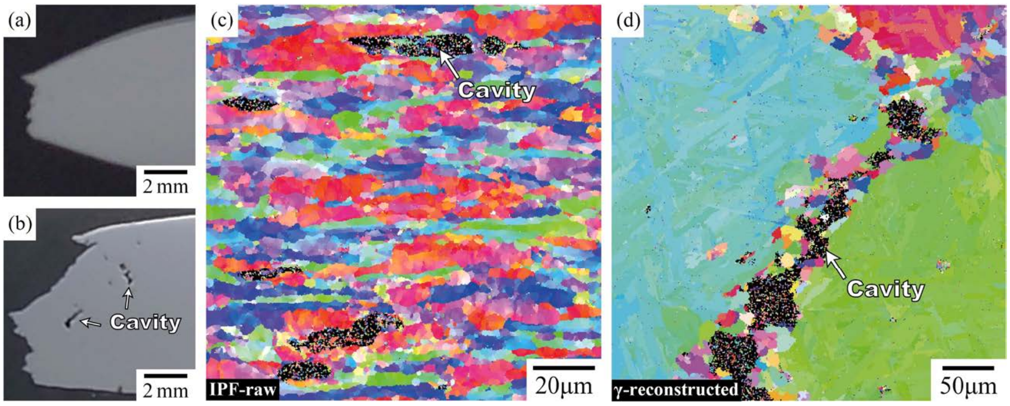

Fig. 3. Scanning electron micrographs (a, b), EBSD-IPF map (c), and γ-reconstruction map (d) taken near the tip of the longitudinally sectioned specimens crept and ruptured at 650°C under 60 MPa for MGQ (a, c) and MGS (b, d). (Online version in color.)

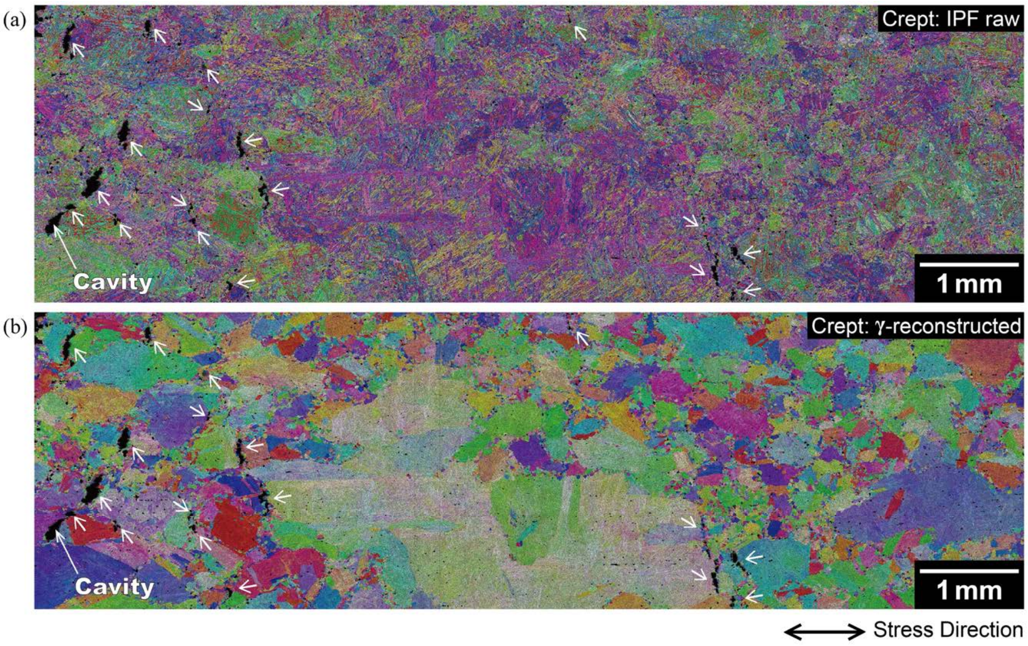

Fig. 4. An extensive area of EBSD-IPF map (a) and the corresponding γ-reconstruction map (b) of MGS specimen fractured at 60 MPa and 650°C. (Online version in color.)

3.3. Metallographic Analysis on Precipitates

As noted above, MGS exhibits an inhomogeneous grain structure consisting of normal and abnormal-sized PAG regions, and the creep cavitation occurred mainly at the normal-sized PAG region. To clarify the differences in the microstructural features between the normal and abnormal PAG regions, quantitative microstructure analysis was done separately for both regions. Although the resolution of the low-voltage SEM is high enough to visualize MX precipitates formed in ferritic steels with a size as small as 10 nm,[13] $M_{23}C_6$ and MX were found to be indistinguishable only from their contrast in the SEM. Therefore, in this study, the size and number density of these precipitates were evaluated without distinguishing between the two.

Figure 5 shows the low-voltage SEM micrographs of as-received and crept specimens showing both the normal and abnormal-sized PAG regions developed in MGS. The number densities of the precipitates formed in both regions are summarized in **Table 2**. For comparison, the results of the specimen tested at 600°C under 100 MPa, of which microstructures are not shown in Fig. 5, are also included in Table 2. Many precipitates of different sizes were observed within the laths as well as on the PAG and block boundaries of the as-received and crept samples (Figs. 5(a), 5(b)). The precipitates formed within the laths with sizes in several tens of nm are MX, while the relatively larger precipitates formed on the block boundaries are primarily $M_{23}C_6$. The precipitates showing the highest contrast in the crept specimens were Laves phase. In addition, the bright circular rims that are particularly notable in the crept specimens correspond to surface artifacts (depressions) introduced during surface finishing by ion milling. What is interesting is that the precipitate number density in the normal-sized PAG region was lower than in the abnormal-sized PAG regions in the as-received materials. This trend is further pronounced in the crept samples, as shown in Fig. 5(d).

Figure 6 shows the frequency distributions (a, b) and the normal probability plot (c) for carbide diameter distribution in the normal and abnormal-sized PAG regions of the specimen ruptured at 650°C under 60 MPa. Figure 6 depicts that

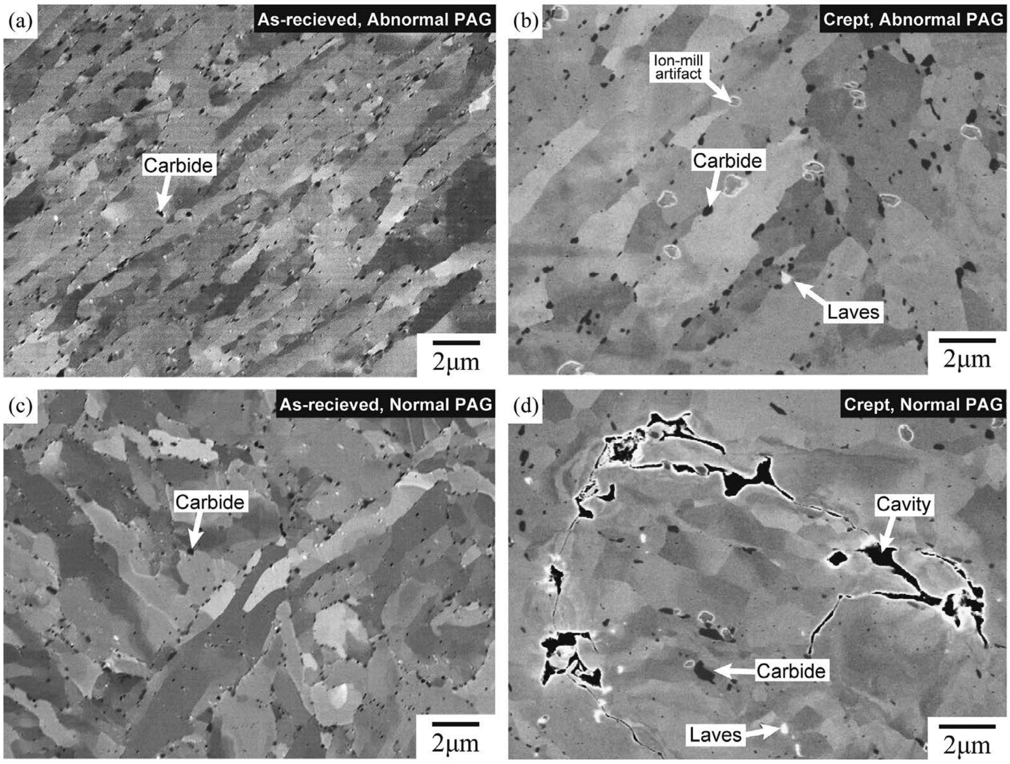

Fig. 5. Low-voltage SEM micrographs of MGS for the as-received (a, c) and the crept (b, d) specimens showing the abnormal-sized PAG region (a, b), and the normal-sized PAG region (c, d).

Table 2. Summary of the number density of precipitates and micro-Vickers hardness value.

Heat	Condition	Area	Precipitate Number Density [μm^{-2}]	Vickers Hardness [HV]
MGQ	As-received		2.26	237 ±8
MGS	As-received	Normal sized PAG	2.10	233 ±2
		Abnormal sized PAG	2.64	237 ±7
	Crept at 600°C for 55 185 h under 100 MPa	Normal sized PAG	0.51	187 ±3
		Abnormal sized PAG	0.68	192 ±1
	Crept at 650°C for 38 108 h under 60 MPa	Normal sized PAG	0.36	165 ±2
		Abnormal sized PAG	0.57	184 ±9

the distributions of the precipitate size in both the normal and abnormal-sized PAG regions of the crept MGS specimen are quite similar. The mode of distribution (the value that appears most frequently in the dataset) is 63 nm in the abnormal-sized PAG region, and the same value is found in the normal-sized PAG region (Figs. 6(a), 6(b)). In addition, the probability plots for the precipitate size distribution in both normal and abnormal-sized PAG regions shown in Fig. 6(c) agree with each other. Furthermore, the median of the precipitate size distribution (the middle value in the dataset) is 87 nm for both normal and abnormal PAG regions. These results suggest that the difference in the number densities of precipitates between the normal and abnormal-sized PAG regions is not due to differences in the precipitate size or distribution but rather to variations in the volume fraction of the precipitates.

Figure 7 shows BF-STEM images and corresponding EDS maps for Cr and V obtained from an abnormal-sized

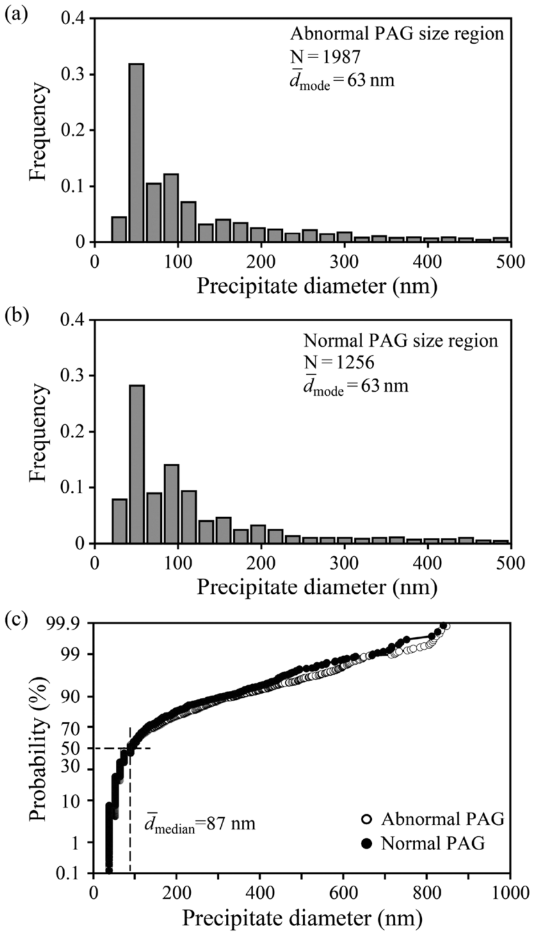

Fig. 6. Frequency distributions (a, b) and normal probability plot (c) for carbide diameter distributions in the normal-sized PAG region and the abnormal-sized PAG region of the specimen crept and ruptured at 650°C under 60 MPa.

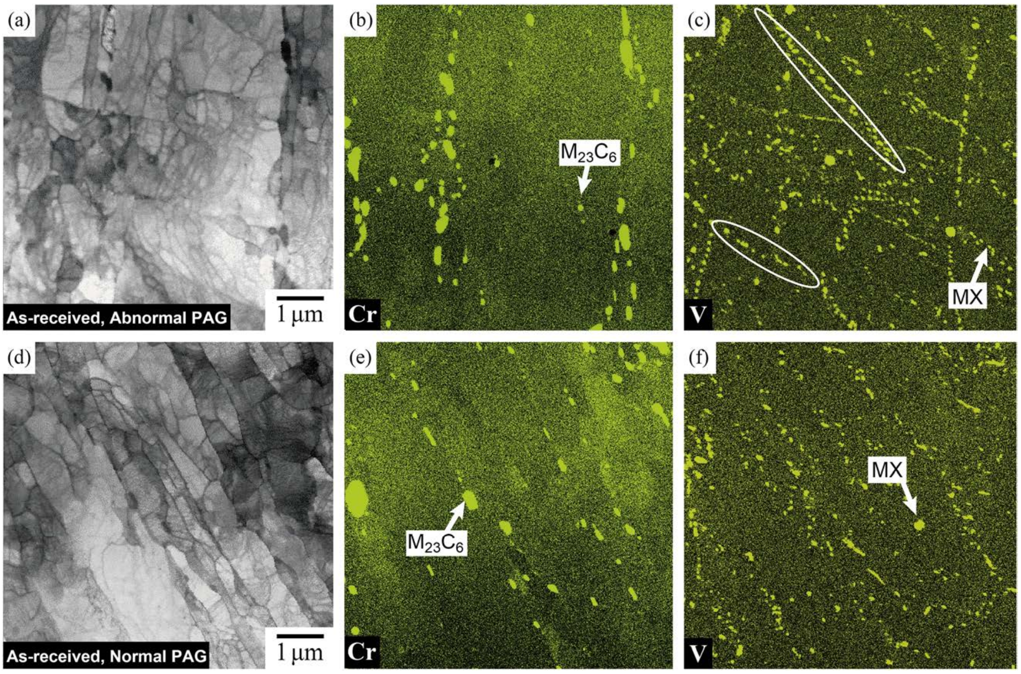

Fig. 7. BF-STEM micrographs (a, d), and EDS elemental maps of Cr (b, e) and V (c, f) from the abnormal-sized PAG region (a–c) and the normal-sized PAG region (d–f) of the as-received MGS. (Online version in color.)

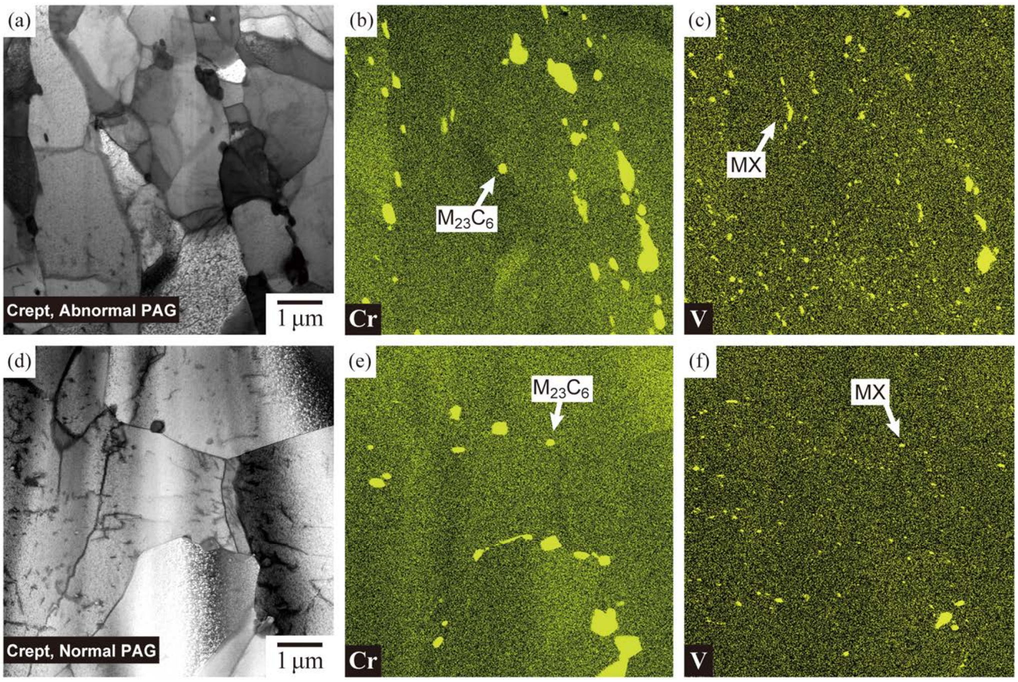

Fig. 8. BF-STEM micrographs (a, d), and EDS elemental maps of Cr (b, e) and V (c, f) from the abnormal-sized PAG region (a–c) and the normal-sized PAG region (d–f) of the MGS specimens crept and ruptured at 650°C under 60 MPa. (Online version in color.)

PAG region (a–c) and a normal-sized PAG region (d–f) of the as-received MGS sample. The Cr- and V-enriched areas correspond to $M_{23}C_6$ and MX precipitates, respectively. $M_{23}C_6$ predominantly precipitated along block boundaries in both regions. In contrast, MX precipitates were formed not only along the lath and block boundaries but also within the lath interiors. What is interesting is that rows of agglomerated MX precipitates are observed within the lath interiors, where no boundaries are present, as indicated by circles in Fig. 7(c). It is speculated that these rows of MX precipitates had originally formed along some boundaries and were not fully dissolved into the austenite matrix during the normalizing process. This observation indicates that a homogeneous dispersion of MX precipitates was not achieved during the normalizing process.

Figure 8 shows BF-STEM micrographs obtained from the normal and abnormal-sized PAG regions of MGS specimens crept at 650°C under 60 MPa. The Cr-enriched areas in the EDS map correspond to $M_{23}C_6$ and the V-enriched areas to MX. The amount of precipitates in the normal-sized PAG region is smaller than that in the abnormal-sized PAG region, particularly for MX. Recovery of substructures appears to have proceeded more in the normal-sized PAG region, as shown in Fig. 8, probably due to the smaller number density of the precipitates.

3.4. Vickers Hardness Test

Micro-Vickers hardness was measured in both the normal and abnormal-sized PAG regions of the specimens before and after the creep tests. Table 2 summarizes the results of the micro-Vickers hardness measurements on the normal and abnormal-sized PAG regions of the as-received MGS specimen, as well as the specimens crept at 600°C for 55 185 h under 100 MPa, and at 650°C for 38 108 h under 60 MPa. The hardness of the as-received MGQ was also listed for comparison. The sizes of the residual indents were approximately 10 μm, which is larger than the martensite blocks but smaller than the PAGs. This indicates that the measured hardness values are primarily influenced by microstructural factors, such as martensite blocks and carbide precipitates, rather than packet or PAG size.

In the as-received condition, MGQ and MGS exhibit comparable hardness in both the normal and abnormal-sized PAG regions. As shown in Fig. 2, the sizes of martensite blocks for MGQ and MGS are comparable in the as-received condition. This suggests that, in the as-received condition, the hardness is primarily controlled by the dislocation density within the martensite microstructures, and that the effect of slight differences in block size and precipitate number density between MGQ and MGS on hardness would be marginal. In the crept specimens, on the other hand, the hardness differs significantly between the normal and abnormal-sized PAG regions. These results suggest that recovery has progressed more rapidly in the normal-sized PAG regions than in the abnormal PAG regions. This consideration is supported by the STEM results shown in Fig. 8, where the number of precipitates is lower in the normal-sized PAG regions of the crept MGS samples.

4. Discussions

EBSD examinations suggested the formation of abnormal-sized PAGs (extraordinarily coarsened prior austenite grains of several hundred micrometers), along with normal-sized PAGs of about 20 μm. This inhomogeneous PAG size distribution was found to have a significant impact on creep properties. Creep deformation was localized in the normal-sized PAG regions to form cavities, as shown in Figs. 3 and 4, which led to premature cracking and thereby a smaller reduction of area upon failure. In addition, such localization of creep deformation accounts for the smaller elongation to failure of MGS, since a significant portion of the entire specimen is composed of the abnormal-sized PAG regions that can yield only small deformations.

The localization of creep deformation in the normal-sized PAG region can be attributed to its lower hardness (Table 2), which is partly caused by the lower precipitate number density in this region. Since precipitates act as obstacles to sub-boundary migration and impede recovery and grain growth, the recovery of sub-boundaries progresses more rapidly in the normal-sized PAG regions compared to the abnormal PAG regions, as shown in Fig. 8. In addition, it is well known that the creep rupture life of Gr. 91 steel is sensitive to PAG size, with smaller PAG sizes resulting in shorter creep rupture lives.[24] In this context, the localization of creep deformation in the “normal-sized PAG regions,” with their relatively smaller PAG size, would be reasonable.

An open question is the mechanism behind the formation of the abnormal-sized PAGs in MGS. There might be several possibilities, but it is difficult to verify all of them because detailed information on the manufacturing process is undisclosed. One potential explanation is that the degree of deformation during pipe-forming was too small or the process temperature was too low, so recrystallization did not occur homogeneously and a coarse solidification microstructure remained partially after hot rolling and cooling. As noted above, MGQ and MGS are both steel pipes, but the wall thickness of MGS is much thicker than that of MGQ, implying that the degree of deformation in MGS was possibly smaller. Besides, it has been reported that recrystallization did not occur uniformly in Mod. 9Cr-1Mo steel when the process temperature is low.[25]

Another possible explanation would be abnormal grain growth that could have occurred during the pipe-forming process or during normalizing. The mechanisms of the abnormal grain growth have not been entirely elucidated,[26,27] but are often discussed from the viewpoint of texture, inhomogeneous dislocation density, and dissolution of a second phase.[27–32] In some materials, in which textured microstructures have developed, grains with relatively large misorientations exhibit high grain boundary mobility, leading to abnormal growth.[30] However, such textured PAG microstructures were not confirmed in the present steel specimens. Localized deformation can induce the development of inhomogeneous dislocation density within materials. This could occur when the degree of deformation during pipe forming is insufficient, resulting in spatially inhomogeneous nucleation of recrystallization and the subsequent formation of coarse grains. It has been demonstrated that achieving a certain critical value of equivalent plastic strain is necessary to prevent the formation of such coarse grains.[33] Furthermore, abnormal grain growth can be caused by non-uniform dispersion of MX precipitates. In Mod. 9Cr-1Mo steel, a small amount of MX particles are usually left undissolved in the austenite matrix during normalizing to prevent excessive coarsening of austenite grains. However, if the dispersion of MX was non-uniform due to some segregation or insufficient normalizing, abnormal grain growth could be induced. In fact, rows of agglomerated MX precipitates that did not dissolve into the austenite matrix during normalizing were observed in MGS, as shown in Fig. 7. Nevertheless, no clear evidence was found in this study to fully explain the formation of extraordinarily coarsened PAGs in MGS.

Another open question would be why the number density of carbide precipitates is lower in the normal-sized PAG regions than in the abnormal-sized PAG region. Since the precipitate size distributions are similar in both the normal and abnormal-sized PAG regions, as shown in Fig. 6, the difference in the number density is not caused by the difference in the coarsening behaviors but rather by variations in the volume fractions of the precipitates in the two regions. As shown in Fig. 7, rows of agglomerated MX precipitates are observed within the lath interiors, where no boundaries are present in MGS. This inhomogeneity was probably caused by insufficient normalizing, which may lead to fluctuations in the volume fraction of MX precipitates formed during tempering following the normalizing process. In this context, the inhomogeneous elemental distribution that developed during normalizing would likely involve MX-forming elements, such as V and Nb. It should be noted that Cr solidification segregation has been reported to cause non-uniform distribution of $M_{23}C_6$ precipitates in Mod. 9Cr-Mo steel, leading to long-term degradation of creep strength,[34,35] however, such Cr segregation was not observed in both regions in the present study.

The present study has demonstrated that inhomogeneous PAG microstructures can lead to creep deformation localization and creep ductility reduction. This finding suggests that implementing new standards to regulate microstructural factors, such as the size and uniformity of austenite grains is desirable for enhancing the reliability of thermal power plants.

5. Conclusions

The microstructures of two heats of Mod. 9Cr-1Mo steel showing comparable creep strength but different creep ductility were analyzed to identify factors that can reduce creep ductility. The critical difference between the microstructures of the two heats was the size and distribution of prior austenite grains (PAGs). In the heat with higher creep ductility, the PAGs were uniform in size, approximately 20 μm. In contrast, the microstructure of the heat with lower creep ductility is characterized as a mixture of normal-sized PAGs and abnormal-sized PAGs. Creep deformation was localized in the regions with normal-sized PAG regions, leading to the development of creep cavities and cracks and thus reduced creep ductility. The inhomogeneous size distribution of PAGs along with the presence of extraordinarily coarsened PAGs was found to be a factor that can reduce creep ductility of Mod. 9Cr-1Mo steel.

Statement for Conflict of Interest

The authors declare no conflicts of interest regarding this manuscript.

Acknowledgment

Part of this study was financially supported by JSPS KAKENHI Grant Numbers JP23K23069 and JP22K14504. The authors express their gratitude to Mr. Yasushi Taniuchi, Dr. Kaoru Sekido, and Mr. Takehiro Nojima of the Research Network and Facility Services Division at NIMS for their assistance with the creep testing. Special thanks are also extended to Mr. Taku Moronaga, Ms. Yuka Hara, and Ms. Akiko Nakamura from the same division at NIMS for their technical assistance with microstructure characterization.

REFERENCE

1) F. Masuyama: *ISIJ Int.*, **41** (2001), 612. https://doi.org/10.2355/isijinternational.41.612
2) F. Abe: *Curr. Opin. Solid State Mater. Sci.*, **8** (2004), 305. https://doi.org/10.1016/j.cossms.2004.12.001
3) K. Maruyama, K. Sawada and J. Koike: *ISIJ Int.*, **41** (2001), 641. https://doi.org/10.2355/isijinternational.41.641
4) M. Taneike, F. Abe and K. Sawada: *Nature*, **424** (2003), 294. https://doi.org/10.1038/nature01740
5) K. Sawada, H. Kushima and K. Kimura: *ISIJ Int.*, **46** (2006), 769. https://doi.org/10.2355/isijinternational.46.769
6) J. Hald: *Steel Res.*, **67** (1996), 369. https://doi.org/10.1002/srin.199605503
7) M. A. Gonzalez-Salazar, T. Kirsten and L. Prchlik: *Renew. Sustain. Energy Rev.*, **82** (2018), 1497. https://doi.org/10.1016/j.rser.2017.05.278
8) M. Kimura, K. Kobayashi and K. Yamaguchi: *Tetsu-to-Hagané*, **87** (2001), 508 (in Japanese). https://doi.org/10.2355/tetsutohagane1955.87.7_508
9) K. Sawada, K. Kimura, F. Abe, Y. Taniuchi, K. Sekido, T. Nojima, T. Ohba, H. Kushima, H. Miyazaki, H. Hongo and T. Watanabe: *Sci. Technol. Adv. Mater.*, **20** (2019), 1131. https://doi.org/10.1080/14686996.2019.1697616
10) NIMS Creep Data Sheet No.43A, National Institute for Materials Science, Tsukuba, (2014). https://doi.org/10.11503/nims.1047
11) K. Kimura and K. Sawada: *Mater. High Temp.*, **39** (2022), 538. https://doi.org/10.1080/09603409.2022.2058230
12) J. A. Siefert, J. D. Parker and I. J. Perrin: ASM-EPRI 10th International Conference on Advances in Materials Technology for Power Plants, ASM International, (2024), 969.
13) N. Sekido, N. Kamikawa, K. Tsuzaki, T. Ohmura, T. Hara, G. Miyamoto and T. Furuhara: *Materia Jpn.*, **55** (2016), 593 (in Japanese). https://doi.org/10.2320/materia.55.593
14) F. A. Leckie and D. R. Hayhurst: *Acta Metall.*, **25** (1977), 1059. https://doi.org/10.1016/0001-6160(77),90135-3
15) M. F. Ashby and B. F. Dyson: Advances in Fracture Research (Fracture 84), ed. by S. R. Valluri *et al.*, Pergamon, (1984), 3.
16) B. Wilshire and H. Burt: *Int. J. Press. Vessel. Pip.*, **85** (2008), 47. https://doi.org/10.1016/j.ijpvp.2007.06.002
17) ASME Boiler & Pressure Vessel Code Cases, BPV-S6-2021 Code Case 3048, American Society of Mechanical Engineers (ASME), NY, (2022).
18) C. Cayron, B. Artaud and L. Briottet: *Mater. Charact.*, **57** (2006), 386. https://doi.org/10.1016/j.matchar.2006.03.008
19) G. Miyamoto, N. Iwata, N. Takayama and T. Furuhara: *Acta Mater.*, **58** (2010), 6393. https://doi.org/10.1016/j.actamat.2010.08.001
20) C. Ranger, V. Tari, S. Farjami, M. J. Merwin, L. Germain and A. Rollett: *Metall. Mater. Trans. A*, **49** (2018), 4521. https://doi.org/10.1007/s11661-018-4825-7
21) F. Barcelo, J. L. Bechade and B. Fournier: *Phase Transitions*, **83** (2010), 601. https://doi.org/10.1080/01411594.2010.502054
22) G. V. Kurdjumov and G. Sachs: *Z. Phys.*, **64** (1930), 325.
23) Z. Nishiyama: *Sci. Rept. Tohoku Univ.*, **23** (1934), 325.
24) K. Maruyama, N. Sekido, K. Yoshimi and Y. Yamamoto: *J. Press. Vessel Technol.*, **142** (2020), 061505. https://doi.org/10.1115/1.4047442
25) A. Matsuzaki, Y. Saito, O. Watanabe, C. Shiga and I. Nakagawa: *Tetsu-to-Hagané*, **76** (1990), 1108 (in Japanese). https://doi.org/10.2355/tetsutohagane1955.76.7_1108
26) R. Pei, S. Korte-Kerzel and T. Al-Samman: *J. Mater. Sci. Technol.*, **50** (2020), 257. https://doi.org/10.1016/j.jmst.2020.01.014
27) J. Humphreys and M. Hatherly: Recrystallization and Related Annealing Phenomena, 2nd ed., Elsevier, Oxford, (2004), 3. ISBN 978-0080441641
28) M. Hillert: *Acta Metall.*, **13** (1965), 227. https://doi.org/10.1016/0001-6160(65),90200-2
29) J. Harase, R. Shimizu, K. Takashima and T. Watanabe: *Trans. ISIJ*, **27** (1987), 965. https://doi.org/10.2355/isijinternational1966.27.965
30) F. J. Humphreys: *Acta Mater.*, **45** (1997), 4231. https://doi.org/10.1016/S1359-6454(97),00070-0
31) A. D. Rollett and W. W. Mullins: *Scripta Mater.*, **36** (1997), 975. https://doi.org/10.1016/S1359-6462(96),00501-5
32) M. A. Razzak, M. Perez, T. Sourmail, S. Cazottes and M. Frotey: *ISIJ Int.*, **52** (2012), 2278. https://doi.org/10.2355/isijinternational.52.2278
33) J. Yanagimoto, K. Karhausen, A. J. Brand and R. Kopp: *J. Manuf. Sci. Eng.*, **120** (1998), 316. https://doi.org/10.1115/1.2830129
34) K. Sawada, K. Sekido, K. Kimura, K. Arisue, M. Honda, N. Komai, N. Fukuzawa, T. Ueno, N. Shimohata, H. Nakatomi, K. Takagi, T. Kimura, K. Nomura and K. Kubushiro: *Tetsu-to-Hagané*, **105** (2019), 433 (in Japanese). https://doi.org/10.2355/tetsutohagane.tetsu-2018-066
35) K. Sawada, K. Sekido, K. Kimura, K. Arisue, M. Honda, N. Komai, N. Fukuzawa, T. Ueno, N. Shimohata, H. Nakatomi, K. Takagi, T. Kimura, K. Nomura and K. Kubushiro: *ISIJ Int.*, **60** (2020), 382. https://doi.org/10.2355/isijinternational.isijint-2019-358